MorphoCellSorter: An Andrews plot-based sorting approach to rank microglia according to their morphological features.

Running title: MorphoCellSorter

Sarah Benkeder[1,2], Son-Michel Dinh[2,3], Paul Marchal[1,2], Priscille De Gea[1,2], Muriel Thoby-Brisson[4], Violaine Hubert[1,5], Ines Hristovska[1,2], Gabriel Pitollat[4], Kassandre Combet[1,2], Laura Cardoit[4], Bruno Pillot[1,5], Christelle Léon[1,5], Marlène Wiart[5,6], Serge Marty[7], Jérôme Honnorat[1,2,8], Olivier Pascual[1,2#], Jean-Christophe Comte[1,9 #]

[1] Claude Bernard Lyon 1 University, Lyon, France.

[2] Institut MeLiS, INSERM U1314 CNRS UMR5284, Lyon, France.

[3] Institut National des Sciences Appliquées (INSA), Lyon, France.

[4] Institut de Neurosciences Cognitives et Intégratives d'Aquitaine, CNRS UMR 5287, Université de Bordeaux, Bordeaux, France.

[5] CarMeN Laboratory, INRAE U1397, INSERM U1060, Claude Bernard Lyon 1 University, Lyon France.

[6] CNRS, Lyon, France.

[7] Sorbonne Université, Institut du Cerveau – Paris Brain Institute – ICM, Inserm, CNRS, APHP, Hôpital de la Pitié Salpêtrière, Paris, France.

[8]French Reference Center on Paraneoplastic Neurological Syndromes and Autoimmune Encephalitis, Hospices Civils de Lyon.

[9] Centre de Recherche en Neurosciences de Lyon (CNRL), INSERM 1028 CNRS UMR5292, Bron, France.

[#] Contributed equally

Key words Microglia; Morphology; Andrews plots; Principal component analysis; Ranking; Ischemia; Alzheimer's disease; Development; Neurodevelopmental disease.

Word count: 10620

Abstract

Microglia exhibit diverse morphologies reflecting environmental conditions, maturity or functional states. Thus, morphological characterization provides important information to understand microglial roles and functions. Most recent morphological analysis relies on classifying cells based on morphological parameters. However, this classification may lack biological relevance, as microglial morphologies represent a continuum rather than distinct, separate groups, and do not correspond to mathematically defined, clusters irrelevant of microglial cells function. Instead, we propose a new open-source tool, MorphoCellSorter, which assesses microglial morphology by automatically computing morphological criteria, using principal component analysis and Andrews plots to rank cells. MorphoCellSorter properly ranked cells from various microglia datasets in mice and rats of different age, from *in vivo*, *in vitro* and *ex vivo* models, that were acquired using diverse imaging techniques. This approach allowed for the discrimination of cell populations in various pathophysiological conditions. Finally, MorphoCellSorter offers a versatile, easy and ready-to-use method to evaluate microglial morphological diversity that could easily be generalized to standardize practices across laboratories.

48

49 **Introduction**

50 In the healthy brain, microglial cells are characterized by a complex arborization of highly ramified
51 and fine processes that are distributed around the cell body. Their processes present a strong and
52 constant dynamic of protractions and retractions in the adult (Hristovska et al., 2022). For many
53 years, this dynamic has been associated with their monitoring role, as they are constantly looking for
54 danger signals in their surroundings (Davalos et al., 2005; Nimmerjahn, Kirchhoff, & Helmchen,
55 2005). Microglia continuously adapt to their local environment, sensing even small changes via
56 membrane receptors and transporters (Hanisch & Kettenmann, 2007). They are able to react quickly
57 and adjust their functions in response to the detected signals. These functional changes are
58 supported by morphological modifications. As an example, the formation of filopodia enables
59 directed migration to lesion sites, while the formation of phagocytic cups and phagolysosome
60 increases are linked to their phagocytic activity (Kettenmann, Hanisch, Noda, & Verkhratsky, 2011;
61 Sierra, Abiega, Shahraz, & Neumann, 2013).

62 The traditional view of microglia being either ramified (homeostatic microglia) or amoeboid (reactive
63 microglia) has now been proven to be oversimplified and inaccurate, as microglia display a whole
64 range of various morphologies (Paolicelli et al., 2022). Indeed, many studies have shown a wide
65 diversity of microglial morphotypes in pathological conditions, and microglia can even exhibit an
66 increase in ramification within the first hours of injury (Vidal-Itriago et al., 2022).

67 In stroke models, morphological transformation of reactive microglia is correlated with the severity
68 and duration of ischemia, as well as an enhanced expression of markers such as CD11B and CD68
69 (Zhang, 2019). In the rodent brain, different morphotypes can be observed depending on how the
70 area has been impacted by the ischemic challenge (V. Hubert et al., 2021). Thus, a gradient of
71 microglial morphologies can be observed from amoeboid microglia in the ischemic core to ramified
72 complex cells in the contralateral cortex (Anttila, Whitaker, Wires, Harvey, & Airavaara, 2017;
73 Fumagalli, Perego, Ortolano, & De Simoni, 2013). Similarly, in Alzheimer's disease (AD) mouse

74 models, microglial cells associated with Aβ plaques present strong morphological transformations in
75 opposition to plaque-distant cells mildly morphologically impacted (Plescher et al., 2018).

76 As a matter of fact, morphology is an indicator commonly accessible through live imaging or
77 immunohistochemistry, and it has been used in numerous studies to describe a broad range of
78 pathological contexts (Adeluyi et al., 2019; Ali et al., 2019; Morrison, Young, Qureshi, Rowe, &
79 Lifshitz, 2017; Plescher et al., 2018). To date, the literature contains a wide variety of criteria to
80 quantitatively describe microglial morphology, ranging from descriptive measures such as cell body
81 surface area, perimeter, and process length to indices calculating different parameters such as
82 circularity, roundness, branching index, and clustering (Adaikkan et al., 2019; Heindl et al., 2018;
83 Kongsui, Beynon, Johnson, & Walker, 2014; Morrison et al., 2017; Young & Morrison, 2018). Artificial
84 intelligence (AI) approaches such as machine learning have also been used to categorize
85 morphologies (Leyh et al., 2021). This variety of metrics and approaches to measure microglia
86 morphology makes it difficult to compare results between studies. Moreover, categorization
87 methods seem subjective with the number, name and composition of categories being non-
88 consistent between studies. In a biological and functional perspective mathematical of manual
89 clustering can be arbitrary as microglia morphology exists along a continuum. In addition, as
90 microglial morphology is highly diverse, it is not rare to be confronted with cells belonging to
91 categories that are not defined, or that could belong to several of them.

92 Here, we propose a fully automated program that quickly and unbiasedly computes most parameters
93 used in the literature to characterize microglial morphology, and overcomes the limitations of
94 current methods. Our approach consists in: 1) performing principal component analyses (PCA) to
95 select the parameters best fitted to describe the dataset of interest and 2) generating a sorting of the
96 cells based on their morphology. The originality of our study is the use of Andrews Plots to rank
97 microglia according to their morphology and discriminate distinct populations. In addition, our
98 working flow has been developed so that it can be used for a wide variety of models and image

acquisitions (confocal, wide field, two-photon, etc.). We developed this method on an exploratory dataset from a rat brain with focal cerebral ischemia, and validated it on other independent datasets from other models (other animal, age, pathology) to confirm its wide range of application.

Methods

Models

All experimental procedures were carried out in accordance with the French institutional guidelines and ethical committee, and authorized by the local Ethics Committees of the University of Bordeaux and "Comité d'éthique pour l'Expérimentation Animale Neurosciences Lyon": CELYNE; CNREEA no. 42, and the Ministry of National Education and Research (APAFIS#30666-2021032518063894).

Ischemic stroke rat model – fixed tissue

The experiment was conducted on 6-8-week-old male Sprague Dawley rat with transient (90 minutes) middle cerebral artery occlusion (tMCAo) followed by reperfusion. Twenty-four hours after reperfusion, the animal was deeply anesthetized (xylazine at 12 mg/kg and ketamine at 90 mg/kg in 0.9% NaCl) and died by the collapse of the lungs when the thoracic cage was open. Infusion of phosphate-buffered saline (PBS) was performed directly in the left ventricle. Next, 100 mL of paraformaldehyde (PFA) 4% was infused at 10 mL/min before the brain collection. The brain was then post-fixed in PFA 4% for 2-4 days, rinsed, and soaked in 30% sucrose for 72 hours before being frozen in -40°C 2-methylbutane. It was then stored at -20°C until being cut. Floating 30 µm thick sections were obtained using an NX50 cryostat and conserved in PB-Thimerosal until immunostaining.

Ischemic stroke mouse model – live tissue

An ischemic stroke was induced in 8 to 12 weeks CX3CR1$^{+/GFP}$ male mice (RRID:IMSR_JAX:005582) by a permanent occlusion of their middle cerebral artery (pMCAo). Imaging was performed the next day

122 directly on living animals through a cranial window. Briefly, animals were anesthetized with
123 isoflurane (induction: 3-4%, surgery: 1.5-2%) and installed on a stereotaxic apparatus where their
124 temperature was monitored and maintained at 37°C. After cleaning and exposition of the skull, a
125 polyamide implant was glued on a zone at the periphery of the lesion in order to be able to image
126 both ischemic and extralesional regions. The skull was then cautiously thinned by drilling until a
127 thickness of 20 to 30 µm was reached. A glass coverslip was then glued to the thinned region. Mice
128 were then put under a heating lamp and individually housed for 24 hours until imaging (V. Hubert et
129 al., 2021).

130

131 *Phox2b mutation and Embryonic dataset*

132 The expansion of a 20-residue polyA tract in PHOX2B is used as a model for Central Hypoventilation
133 Syndrome (CCHS) (Amiel et al., 2003). Mutant pups were generated by mating conditional
134 Phox2b$^{27Ala/27Ala}$ females with Pgk::Cre males (Dubreuil et al., 2008). Since mutant newborns die
135 rapidly after birth, all experiments were performed blind on E18.5 embryos of either sex, and the
136 genotype of each embryo was determined a posteriori on tail DNA. Pregnant mice were killed by
137 cervical dislocation at E18.5. Embryos were rapidly excised from uterine horns and placed in artificial
138 oxygenated cerebrospinal fluid (aCSF) at 18-20°C until dissection. The aCSF solution composition was
139 (in mM): 120 NaCl, 8 KCl, 0.58 NaH2PO4, 1.15 MgCl2, 1.26 CaCl2, 21 NaHCO3, 30 Glucose, pH 7.4 and
140 equilibrated with 95% O_2-5% CO_2. Embryos were decerebrated and decapitated, and ventral tissues
141 were removed. Brainstems were then carefully disassociated from the surrounding tissues and
142 completely isolated by a rostral section made at the junction between the rhombencephalon and
143 mesencephalon and a caudal section at the spinal cord level. After dissection, brainstem
144 preparations were placed in 4% PFA for 2 - 3 h for tissue fixation. To obtain transverse frozen
145 sections, brainstems were placed in a 20% sucrose-PBS solution for cryoprotection overnight, then
146 they were embedded in a block of Tissue Tek (Leica Microsystems, France) and sectioned at 30 µm
147 using a cryostat (Leica Microsystems, France).

148 *Alzheimer's Disease model*

149 C57BL6 5-month-old female APPxPS1-KI and control (PS1-KI) mice were used(Casas et al., 2004). For
150 the brain collection, 0.5 mg xylazine was injected intraperitoneally followed by Euthasol. They were
151 then intracardially perfused first with 4% PFA in PB. After one hour, the brains were collected and
152 then post-fixed for 2 hours in 4% PFA and stored in PBS. They were rinsed in phosphate buffer (PB)
153 and soaked in 30% sucrose for 48 hours before being frozen at -40°C in 2-methylbutane for 2 minutes
154 and stored at -70°C until the cut. Free-floating sections (30 µm thick) were cut using a cryostat and
155 conserved in PB-Thimerosal until immunostaining.

156 *In vitro microglia*

157 We followed the protocol published by Bohen and collaborators using Magnetic Activated Cell
158 Sorting (MACS) (Bohlen, Bennett, & Bennett, 2019). Ten days old mice were anesthetized with
159 isoflurane, intracardially perfused with PBS enriched with magnesium and calcium (14040141, Gibco)
160 before decapitation and brain collection. The brains were then finely chopped in a dissociation buffer
161 and transferred to a tissue grinder to dissociate further the cells from the tissue. Myelin and debris
162 were then eliminated thanks to a Percoll® PLUS solution (E0414, Sigma-Aldrich) diluted with DPBS10X
163 (14200075, Gibco) and enriched in $MgCl_2$ and $CaCl_2$ (for 50 mL of myelin separation buffer: 90 mL of
164 Percoll PLUS, 10 mL of DPBS10X, 90 µL of 1 M $CaCl_2$ solution, and 50 µL of 1 M $MgCl_2$ solution). An
165 incubation with anti-myelin magnetic beads (130-096-433, Miltenyi Biotec): the cell suspension is
166 applied on a column fixed to a magnet so that the myelin will stay on the column while the cells will
167 exit. To isolate specifically microglia, the suspension was incubated with anti-CD11b magnetic beads
168 (130-097-142, Miltenyi Biotec). 20.000 cells were then seeded on each of the four compartments of
169 the 35 mm diameter dishes with a polymer bottom (80416, Ibidi) coated with poly-D-lysine (100
170 µg/mL, A-003-E, Sigma-Aldrich) and collagen IV (2µg/mL, 354233, Corning). The culture medium was
171 adapted from Bohlen et al., 2019 with DMEM/F12 (21041025, Gibco), 1% penicillin-streptomycin, 2
172 mM L-Glutamine (10378016, Gibco), 5 µg/mL N-acetylcysteine (A9165, Sigma-Aldrich), 100 µg/mL

173 apo-transferrin (T1147, Sigma-Aldrich), 100 ng/mL de sodium selenite (S5261, Sigma-Aldrich), 1.5
174 µg/mL cholesterol (700000P, Avanti), 0.1 µg/mL oleic acid (90260, Cayman Chemical), 1 ng/mL
175 gondoic acid (20606, Cayman Chemical), 1 µg/ml heparan sulfate (AMS.GAG-HS01, AMSBIO), 2
176 ng/mL TGFβ2 (100-35B, Preprotech) and 10 ng/mL M-CSF (315-02, Preprotech). Cells were kept at
177 37°C 5% CO_2 and the culture medium was half renewed every two days until imaging (4 to 10 days
178 after seeding).

179 **Immunohistochemistry**

180 The sections underwent 5-minute rinses three times with PBS and Triton 100X 0.3% (PBS-T). Sections
181 from the ischemic experiment were incubated for 20 minutes in a 1.5% hydrogen peroxide solution
182 diluted in PBS, and after 3*10 minutes of rinsing with PBS-T, they were incubated for 30 minutes in
183 0.5% sodium borohydride diluted in PBS and then thoroughly rinsed. One-hour saturation was then
184 performed on all sections with PBS-T, 3% bovine serum albumin and 5% normal goat serum (PBS-T-
185 BSA-NGS). Sections were then incubated overnight with anti-Iba1 antibodies (1/500, Wako, Germany,
186 #W1W019-19741) at 4°C and anti-Amyloid-β 4G8 (1/500, Bio-Legend, #800709) antibody. Sections
187 were rinsed 3*10 minutes the next day with PBS-T. They were then incubated in goat anti-rabbit
188 secondary antibodies coupled with Alexa 555 fluorochrome (1/300, Invitrogen, France, #A21429) and
189 goat anti-mouse coupled with Alexa 488 fluorochrome (1/300, Invitrogen, France, #A11029) for 2
190 hours at room temperature. They were then rinsed 3*10 minutes with PBS and mounted on
191 microscope slides using Fluoromount G (ThermoFisher Scientific, #00-4958-02) and a glass coverslip.

192 For the Phox2b mutant model and embryonic dataset, sections were incubated for 90 min in a
193 solution of PBS containing 0.3% Triton X-100 and 1% BSA to limit nonspecific labeling and favor
194 antibody tissue penetration. The primary rabbit anti-Iba1 antibody (1/500; Wako, Germany,
195 #W1W019-19741) was then applied overnight at room temperature and under slight agitation. To
196 amplify the primary antibody signal, after several washes, sections were incubated with an Alexa
197 Fluor 568 donkey anti-rabbit secondary antibody (1/500, Merck, France, #A10042) for 90 min at

198 room temperature. Immunostained sections were then mounted in Vectashield Hard Set medium
199 (Eurobio, France) cover-slipped and kept in the dark until imaging.

200 **Image acquisitions**

201 For the ischemic stroke model on fixed tissue, acquisitions were performed with a Zeiss confocal
202 microscope and a 40X objective (LSM 880, Zeiss). Z-stacks between 18 and 25 µm thickness were
203 executed with a 1 µm step. For the ischemic stroke model on live, microglia were observed thanks to
204 a two-photon microscope (Bruker Ultima) and a 20X objective, at a deepness of 50 to 150 µm. 10 to
205 15 µm thick acquisitions were acquired with a 1 µm step between plans. For the AD model, a Zeiss
206 Axio Scan 7 microscope slide scanner was used with a 20X objective. Z-stacks (30 µm thick) were
207 performed with a step of 1 µm. For the Phox2b mutant model, imaging was conducted using a Zeiss
208 confocal microscope (LSM 900, Zeiss). Z-stacks (30 µm thick) were performed with a step of 1 µm and
209 a 40X objective. *In vitro* microglia were imaged on a single plane using the BioStation (Nikon).

210 **Image processing and segmentation**

211 The general procedure is described in supplemental Fig. 7.

212 For the ischemic model on fixed tissue, all post-acquisition processing was executed with FIJI
213 software (2.9.0/1.54f). Individual microglial cells were cropped from the original acquisitions before
214 Z-maximum projections. The brightness of the projections was adjusted, and median (radius=2),
215 mean (radius=2) and unsharp mask (radius=5; mask=0.60) filters were applied via a macro. A
216 threshold was then applied to each crop to binarize the cells, and pixels not belonging to the
217 microglia of interest were manually deleted. The same procedure was performed for the Phox2b
218 mutant model, except the mean filter that was not applied.

219 For the ischemic model on live tissue all post-acquisition processing was also executed with FIJI
220 software. Z-maximum projections were performed, and individual crops of the cells were done.

221 Brightness and contrast of the images were modified before applying a manual threshold to binarize
222 the cells. Reminiscent noise and neighboring cells were manually removed.

223 For the AD model, crops of individual microglial cells located in the secondary visual cortex were
224 extracted from images using the *Zen* software (v3.5; Zeiss) and exported to the Tif image format. The
225 next operations were executed with FIJI software. Z stack cleaning was performed by background
226 subtraction (rolling=50), followed by a median filter (radius=3) and an unsharp mask (radius=5;
227 mask=0.60). Segmentation was performed by the FIJI Trainable Weka Segmentation 3D plugin
228 (Arganda-Carreras et al., 2017). The selected training features were based on the Gaussian blur,
229 Laplacian, Maximum, Mean, Minimum, Median and Variance (Minimum sigma: 1.0 and Maximum
230 sigma: 8.0). Binarized z-stacks were then manually cleaned to remove pixels from neighboring cells or
231 remaining noise. Finally, a maximum Z-projection was performed.

232 For the Phox2b mutant model, image processing was performed via a custom MATLAB R2018B
233 (Mathworks, Massachusetts, USA) script. First, a median filter followed by an unsharp mask filter was
234 applied to all images. An automated threshold was then applied. Manual tuning with a thresholding
235 tool (R, 2023) was applied if the automated threshold was not satisfying. The binarized images were
236 then automatically cropped around microglia. Briefly, the centroid of each detected object (i.e.
237 microglia), except the ones on the borders, were detected, and a crop of 300x300 pixels around the
238 objects were generated. Then, the pixels belonging to neighboring cells were manually removed on
239 each generated crop.

240 For the *in vitro* microglia, acquisitions were cropped around individual microglia, and the cells were
241 then manually traced on Procreate (5.2.9 version).

242 When the binarization process generated one or several holes inside the cell bodies, they were
243 manually filled to not interfere with the automated detection of the cell bodies. All binarized and
244 individualized microglial cells were then rescaled through a FIJI macro command to obtain a pixel

245 resolution equal to 0.5 µm. Finally, the images were resized to obtain a field size equal to 300 x 300
246 pixels.

247 **MorphoCellSorter algorithm pipeline**

248 **Automated measure of 20 dimensionless morphological descriptors**

249 All parameters are illustrated in Supp. Fig. 8.

250 First, we calculate the morphological parameters most commonly used in the literature, followed by
251 other parameters that we have developed and proposed here (Fig. 2B). To make our approach scale-
252 independent, we reformulated some morphological descriptors to obtain dimensionless parameters.

$$Circularity = \frac{2 \times \sqrt{\pi \times CellArea}}{CellPerimeter}$$

$$RamificationIndex = \frac{\frac{CellPerimeter}{CellArea}}{2 \times \sqrt{\pi \times CellArea} \times Image\ length \times Image\ width}$$

$$RoundnessFactor = \frac{4 \times SomaArea}{(Longest\ axis\ length)^2 \times \pi}$$

$$PerimeterAreaRatio = \frac{Perimeter^2}{Cell\ Area}$$

$$Density = \frac{CellArea}{Length \times width\ of\ the\ image}$$

$$Inertia = \frac{Longest\ axis\ length}{Smallest\ axis\ length}$$

253

254 *Cell Body Recognition*

255 The cell body identification is based on successive erosions until the center of the cell body is the
256 only pixels remaining using a 3*3 pixels square as a structuring element. The last erosion is the one
257 preceding the elimination of all pixels belonging to the cell and corresponds to the center of the cell
258 body. Then, successive dilations are performed to reconstruct the cell body according to the
259 morphology of the cells, using a cross (+) 3 pixels height and width (Leyh et al., 2021). Reconstruction
260 of the cell body relies on (1) the identification of the index *i* on which measured surfaces after
261 erosions are inferior to the surfaces measured after dilation, (2) the average of two copies of the

images: one on which *i* + 1 erosions have been performed, and the other one on which *i* dilatations have been performed from the center of the cell body. The resulting mean image was then subjected to a threshold fixed at 0.25 to obtain the cell body. From this, we can calculate the following parameters.

$$Processes\ Soma\ Areas\ Ratio = \frac{Processes\ Area}{Soma\ Area}$$

$$Processes\ Cell\ Areas\ Ratio = \frac{Processes\ Area}{Cell\ Area}$$

$$Polarization\ Index = \frac{Soma\ Centroid \mid Cell\ Centroid}{\sqrt{CellArea}}$$

Skeleton

The cell skeleton is obtained via the MATLAB *bwskel* function. This function reduces all 2-D binary objects to 1-pixel width curves while taking care of not changing the essential structure of the image. The aim is to extract the image skeleton while keeping the topology properties such as the Euler number and to extract branchpoints and endpoints. The skeleton length is defined by the number of pixels forming the skeleton minus the pixels of the cell body.

Thus, we calculate the skeleton related parameters:

$$Skeleton\ Process\ Ratio = \frac{(Skeleton\ Length)^2}{Processes\ Area}$$

$$Branchpoints\ Endpoints\ Ratio = \frac{Number\ of\ Branchpoints}{Number\ of\ Endpoints}$$

Sholl analysis

Sholl analysis was performed on the microglial skeleton. Concentric circles with a step size of two pixels were generated on the skeletons minus the soma, and the soma centroid was the center point of the circles. Intersections between the growing circles and the skeleton were counted.

$$Branching\ Index = \sum \frac{(Intersections\ circle_n - \ Intersections\ circle_{n-1}) \times r_n}{\sqrt{Length\ \times width\ of\ the\ image}}$$

Fractal/Hausdorff dimension

The fractal dimension measures the complexity of a cell shape, that is, how an object fills the space at different scales. The Hausdorff fractal dimension (A, 2023) corresponds to the slope of the logarithm of the number of tiles of size ε needed to cover all the surfaces of the object of interest vs the logarithm of ε.

Lacunarity

Lacunarity corresponds to the inhomogeneity of a cell shape. It measures the variance of how the object fills the space at different scales. Patterns with larger gaps generally have higher lacunarity. We used the gliding box algorithm (T, 2023; Tolle, McJunkin, & Gorsich, 2008), and the value corresponds to the slope of the log-log representation.

Convex Hull

The convex hull is the smallest convex polygon (with angles inferior to 180°) enclosing the whole cell.

$$Solidity = \frac{Cell\ Area}{Convex\ hull\ Area}$$

$$Convexity = \frac{Cell\ Perimeter}{Convex\ hull\ Perimeter}$$

$$Convex\ Hull\ Circularity = \frac{2 \times \sqrt{\pi \times Convex\ hull\ Area}}{Convex\ hull\ Perimeter}$$

We also measure the length of the major and minor axes of the convex hull.

$$Convex\ Hull\ Span\ Ratio = \frac{Length\ Major\ axis}{Length\ Minus\ axis}$$

Finally, we measure the largest and smallest radii of the circles from the centroid of the convex hull as the center to external points.

$$Convex\ Hull\ Radii\ Ratio = \frac{Maximum\ Convex\ hull\ radius}{Minimum\ Convex\ hull\ radius}$$

Linearity

299 A Principal Component Analysis is generated on all the points forming the microglial cell. Then, the
300 variance of the two first principal components (PCs) is calculated; the highest corresponds to the
301 Variance Max and the lowest to the Variance Min.

$$Linearity = \frac{Variance\ Max}{Variance\ Min}$$

302

303 **Establishment of the cell ranking according to morphological criteria.**

304 The second step is to determine which of the previously calculated parameters best discriminate the
305 cells in a given dataset. Principal component analysis (PCA) is a statistical method allowing dataset
306 dimensionality reduction (Jolliffe & Cadima, 2016). A PCA is performed on the 20 morphological
307 indexes calculated to determine the parameters that best explain the dispersion of the data.
308 Lacunarity, roundness factor, convex hull radii ratio, processes cell areas ratio and skeleton processes
309 ratio were subjected to an inversion operation in order to homogenize the parameters before
310 conducting the PCA: indeed, some parameters rank cells from the least to the most ramified, while
311 others rank them in the opposite order. By inverting certain parameters, we can standardize the
312 ranking direction across all parameters, thus simplifying data interpretation. To identify the main
313 parameters responsible for the data spreading, we perform a PCA

314 *The principal component 1* (PC_1) is the direction in which data is most dispersed. The two first
315 components represent most of the information (about 70%), hence we can consider the plan PC_1, PC_2
316 as the principal plan reducing the dataset to a two dimensional space. Next, we calculate the
317 projection of the parameters F_n onto the two first principal components respectively PC_1 and $PC2$ (Fig.
318 2C) and rank those parameters according to the intensity (absolute value) of their projection onto PC_1
319 (Fig. 2D). Each parameter is then weighted by a factor $W_n = w_n./w_0$, where w_n is the absolute value of
320 the nth parameter projection onto PC_1, and w_0 is the absolute value of the strongest projection among
321 all the parameters. As shown in Fig. 2C, each parameter F_n is represented by a vector in the PC_1, PC_2.
322 Thus, we calculate the projection y_n of each parameter onto PC_2 and calculate the following phase
323 factor

$\phi_n = arctan(y_n/w_n)$.

The following stage of our method consists in introducing the previously calculated factors (Weight: W_n, and phase: ϕ_n) and their corresponding parameter into a special Fourier synthesis called "Andrews Plot" or "Andrews curve" (Andrews, 1972; García-Osorio & Fyfe, 2005) allowing to visualize the data structure in high-dimensional. The general form of the spectral Fourier synthesis of an individual *j* writes:

$$S_j(t) = \sum_{n=1}^{N} A_n \; cos(2\pi \; n \; t) + B_n \; sin(2\pi \; n \; t) \; , \qquad (4)$$

that we rewrite as,

$$S_j(t) = \sum_{n=1}^{N} C_n \; cos(2\pi \; n \; t \; + \phi_n), \qquad (5)$$

where *n*, is the index of the ranked parameters, *N* is the full number of parameters F_n, *t* is a virtual time $0 \leq t \leq 1$, and $C_n = F_n \times W_n$. Finally, we derive this method to represent data in high dimensional by a simple one-dimension signal composed of orthogonal trigonometric functions in researching the time $t = t^*$ for which the curves present the maximum of variance. At this specific time point, we rank individuals according to the magnitude of their own function $S_j(t^*)$ value as represented Fig. 2E. We now call $S(t^*)$ the "Andrews-Score".

Statistics

Rankings comparisons, performed with Spearman's correlation, were also used to measure the monotonic correlation between the rankings. They were executed with MATLAB.

343 We used mixed effect models on RStudio, that are adapted to complex experimental designs with
344 dependent and non-dependent data. This allows the addition of random factors to fixed effects.
345 Model fittings and analysis were performed with the lme4 package (Amiel et al., 2003). Condition
346 (Control/APP-PS1xKI or WT/CCHS) was considered a fixed effect, and the factor mice was considered
347 a random intercept. When the mixed models were not applicable, we used Wilcoxon tests. Statistical
348 significance is shown on the graphs (*p < 0.05; **p < 0.01; ***p < 0.001).

349 Number of bins of Andrews scores histograms was automatically determined by the Freedman-
350 Diaconis method based on the following formula:

351 $$k = (x_{max} - x_{min})/(2 \times IQR \times N^{(-1/3)})$$

352 With x_{max} and x_{min} being respectively the maximum and minimum Andrews scores, IQR the
353 interquartile range and N the number of cells.

354 **Results**

355 **Evaluation of classification methods**

356 Morphological categorization has been at the center of recently developed approaches to
357 characterize microglial morphology. It enables the evaluation of the morphological diversity existing
358 in a cell population. Moreover, in the context of morphological comparison between populations, the
359 study of the morphotypes' proportions is relevant as it can highlight meaningful differences that the
360 sole global comparison of morphological criteria cannot. One way to categorize the cells based on
361 their morphology is to perform clustering to group the cells having similar characteristics. We tested
362 a commonly used approach, k-means, to categorize microglia from a rat brain cortex following an
363 occlusion of the middle cerebral artery (Fig. 1A). In this model, microglia contralateral to the lesion
364 are mildly to not impaired whereas ipsilateral microglia undergo light to drastic morphological
365 changes (Anttila et al., 2017; Fumagalli et al., 2013) (Fig. 1A). We selected 20 non dimensional
366 parameters from the literature and developed by the team, on which we conducted a Principal

367 Component Analysis (PCA). The k-means clustering algorithm was applied on the first two principal
368 components (PCs), and we fixed at 4 the number of clusters as commonly chosen in the literature
369 (Verdonk et al., 2016) (Fig. 1B).

370 The obtained microglial groups could be named as ramified microglia (cluster 1), with cells having a
371 morphology consistent with a physiological state. Cluster 2 could be referred to as "reactive
372 microglia", as it was composed of microglia displaying various morphologies; they had an
373 intermediary ramification level with large cell bodies. Cluster 3 was composed of cells having few
374 short or no processes and corresponded to amoeboid microglia. Lastly, cluster 4 was rod-like
375 microglia, with two processes extending on either side of the cell body or a single long polarized
376 extension. A sample of the cells of the dataset (ipsilateral and contralateral) and their associated
377 cluster is represented in Fig. 1C. These 4 clusters were not equally represented across each condition
378 as no amoeboid nor rod-like microglia were found in the contralateral side (Fig. 1D). The large
379 majority of the cells were ramified microglia (92%), and the rest were reactive microglia (8%). The
380 proportion of ramified cells drastically decreased ipsilaterally by a reduction factor of 4 (23%), while
381 reactive microglia increased (39%). 25% of the cells were amoeboid microglia, while rod-like cells
382 represented 13% of the ipsilateral population (Fig. 1D). These results show that the microglial
383 populations in each region are different, with microglia having a "non-pathological" morphology
384 mainly found contralaterally, with only few cells being potentially impacted by the
385 ischemia/reperfusion challenge as they showed morphological signs of reactivity with a less ramified
386 morphology. Ipsilateral microglia were morphologically highly altered, with a decrease in ramified
387 cells, replaced by reactive and amoeboid microglia, and rod-like microglia.

388 However, the clusters themselves were highly morphologically heterogeneous, making these
389 quantifications problematic (Fig. 1C). For instance, Cluster 1 (ramified microglia), was composed of
390 cells with branched processes but also included cells that were visibly affected by the ischemic lesion,
391 exhibiting sometimes short, few, or less branched processes, as well as elongated cell bodies. These

392 microglia might have been more appropriate in Cluster 2 (reactive microglia). The composition of the
393 latter is also questionable, with the presence of branched processes that would fit better in the first
394 cluster, or cells with few very short extensions that resemble some cells found in Cluster 3. Several
395 non-bipolar or non-unipolar cells are also found in Cluster 2. We tested to decrease or increase the
396 number of clusters with no improvement (data not shown).

397 Other classification methods exist, relying on supervised artificial intelligence (AI) algorithms to
398 identify specific morphotypes. These approaches can have high rates of success (96% for the method
399 developed by Leyh and collaborators (Leyh et al., 2021)), meaning that they are in theory efficiently
400 classifying cells. However, the problems of cells which do not fit in a defined category, or to several
401 categories can be raised. For example, in our dataset we found that about 60% of cells would not
402 belong to any category or belong to several categories. In this context, the way the networks are
403 trained might be very subjective to the experimenter and could influence the results. Moreover,
404 depending on the papers, semantic problems are also met, with similar morphologies having
405 different names or on the contrary same names having different definitions (Choi et al., 2022; Leyh et
406 al., 2021), making the comparisons between studies complicated.

407 We know now that microglial morphology is rather a continuum than closed categories (Paolicelli et
408 al., 2022). That is why we propose a continuous ranking rather than a classification of the cells.

409

410 **Development of a ranking approach based on Andrews plots to order rat fixed microglia in a**
411 **context of ischemic stroke lesion.**

412 We developed MorphoCellSorter, a novel ranking method, on the same dataset of rat microglia in
413 the context of an ischemic stroke lesion, on fixed tissue acquired *via* confocal imaging. This model is
414 known to induce major morphological modifications in microglia (Violaine Hubert et al., 2021),

enabling us to constitute a heterogeneous dataset, with varied morphologies ranging from amoeboid to hyper-ramified.

The method is summed up on Fig. 2A, and takes as inputs binarized and individualized cells form projected Z stacks. To generate the ranking, we first gathered 20 morphological indices, that we also call parameters, either from the literature (Clarke, Crombag, & Hall, 2021; Fernández-Arjona, Grondona, Granados-Durán, Fernández-Llebrez, & López-Ávalos, 2017; Madry et al., 2018) or developed by the team (see Methods). These parameters, describing morphological complexity (circularity, ramification index, roundness factor, perimeter area ratio, density, processes soma area ratio, processes cell area ration, skeleton processes ratio, branchpoints endpoints ratio, fractal dimension, lacunarity, solidity, convexity, convex hull circularity, convex hull radii ratio and branching index), linearity (linearity, convex hull span ratio, inertia) and directionality (polarization index) of the cells, were normalized to suppress any dimension in order to be exempted from any scale effect. The first step of our method involves PCA, which helps us determine the main parameters responsible for the data dispersion. The first principal component (PC1) captures the direction of maximum variance in the data, and subsequent component (PC2) captures the direction of the next highest variance (Fig. 2B). Typically, the first two principal components account for a significant proportion (often over 70%) of the data's total variance, allowing us to reduce the dataset's complexity to a two-dimensional space, such as a two-dimensional plane defined by PC1 and PC2 (Fig. 2C).

Next, each parameter was projected onto these principal components, which helps us rank parameters based on their influence on the overall data structure (Fig. 2D). To determine the number of parameters used to elaborate the ranking, we selected the median number of the normalized cumulative projection (threshold = 0.5). We assign weights to the selected parameters based on their projections onto PC1, which allows us to emphasize the most influential parameters. This weighted projection, along with phase factors calculated for each parameter (referred as φ_n in the Methods

section), forms the basis of an Andrews Plot — a graphical representation that simplifies high-dimensional data into a two-dimensional signal using trigonometric functions.

The Andrews Plot represents each individual microglia, as a unique curve, allowing for visual comparison based on their trajectories within this synthesized signal (Fig. 2E). This method enables efficient visual comparisons and insights into complex datasets with potentially significant implications for data analysis and interpretation. We took advantage of this representation to rank the cells based on their morphology; the ranking is established at the time point displaying the highest variance, i.e. the time point where the curves are the most dispersed, also named ⍰ (Fig. 2E).

The obtained ranking is displayed on Fig. 3A. To evaluate the quality of the ranking method, we compared the automated ranking to a subjective manual ranking by experts based on visual morphological criteria (cell size; number, length and branching of the processes). To assess the similarity degree between the rankings, we looked at the distribution of rank differences for each microglia between rankings (Fig. 3B) and observed that the majority of the cells' rank differences did not exceed an absolute value of 50 rank difference with a peak around 0. We also calculated Spearman's rank correlation coefficient (r_S=0.96; Fig. 3E). This test revealed that the automated ranking is close to the manual ranking. To ensure the reliability of the manual ranking, we compared the automated ranking with another expert and obtained the same results (r_S=0.97; Fig. 3C,F). Interestingly, the comparison between the two manual rankings shows similar results to those obtained when compared to the automated ranking (r_S=0.93; Fig. 3D,G), indicating that variability is the same between automated or manual rankings. The distribution of the rank differences between the same microglial cells in the two rankings elaborated by the experts even show a greater dispersion of the rank differences, with more cells having rank differences higher than 50 and around 100, showing a part of subjectivity in the cell ranking based on their morphologies. However, automated ranking provided an objective and repeatable result, validating

463 our method. Thus, MorphoCellSorter is able to generate an accurate ranking of the cells based on
464 morphological criteria.

465 **Evaluation of MorphoCellSorter on other datasets of microglia from different animals, age, models**
466 **and imaging techniques**

467 One limitation to the use of a general and common method to characterize microglial morphology is
468 the high diversity of study material: the models (*in vivo*, *ex vivo, in vitro*, fixed or live tissue), the type
469 of collected signal (DAB or fluorescent staining, endogenous fluorescence…), the imaging technique
470 (influencing the resolution and the background noise). We thus wanted to evaluate the capacity of
471 MorphoCellSorter to accurately rank microglia from various datasets having different morphological
472 characteristics (Table 1). As previously, we compared the results to manual rankings performed by
473 two independent experts to evaluate the quality of the automated rankings (Table 1). We tested the
474 accuracy of the rankings using several thresholds impacting the number of parameters selected as
475 entries for the Andrews plots (Table 1). To maximize the accuracy of the automated ranking for all
476 datasets, we determined which threshold provided the best rankings overall (Supp. Table 1). We
477 observed that a threshold of 0.8 (Supp. Table 1), leading to 11 to 12 selected parameters (Supp. Fig.
478 1A-E), constituted a good compromise to obtain good rankings for all datasets. Thus, we chose to fix
479 this threshold for the following analyses. The Andrews plots and rankings obtained at the 0.8
480 threshold are respectively displayed in Supplemental Fig. 2 and 3.

481 Thus, our Andrews plot-based ranking method, relying on an automatic selection of relevant
482 parameters thanks to the PCA, allows a reliable automated ranking of the cells based on their
483 morphologies. The diversity of the tested datasets, with different models, types of signal and imaging
484 techniques shows that our approach offers a good sorting of the cells independently of their shape
485 and context.

486 **APPxPS1-KI microglia in the visual cortex have significant morphological alterations compared to**
487 **control cells.**

488 To determine the usability of our approach to compare microglial morphology in different conditions,
489 we used MorphoCellSorter to assess the presence of morphological alteration in the context of an
490 adult pathological murine model of Alzheimer's disease. This model is known to induce amyloid
491 plaques with dystrophic neurites, synaptic dysfunction and behavioral deficits (Casas et al., 2004).
492 We compared the morphology of PS1-KI (control) and APPxPS1-KI microglia in the visual cortex (Fig.
493 4A). Eleven parameters were automatically selected by the PCA: circularity, ramification index,
494 perimeter area ratio, fractal dimension, skeleton processes ratio, density, convexity, processes cell
495 areas ratio, lacunarity, branching index and processes soma areas ratio (Supp. Fig. 4A-C) and used to
496 generate the Andrews plots (Supp. Fig. 4D). The automated ranking obtained revealed that control
497 and APPxPS1-KI microglia were well segregated with APPxPS1-KI microglia at the beginning of the
498 ranking and control mice at the end (Fig. 4B). The distributions showed a 16.4% overlap between the
499 populations, meaning that a large number of APPxPS1-KI cells have a morphology that differs from
500 that of controls (Fig. 4C).

501 The morphological indices showed significant differences between APPxPS1-KI and control microglia.
502 The parameters measuring the morphological complexity of the cells highlighted a clear decrease in
503 the ramification level of APPxPS1-KI microglia, with for example a fractal dimension and convexity
504 decrease and a circularity increase. However, there were no significant differences in the cells'
505 linearity and polarity between groups (Fig. 4D-W).

506 Thus, this approach allowed the detection of morphological changes of microglia in the visual cortex
507 of APPxPS1-KI mice.

508 **MorphoCellSorter pinpoints no morphological alterations in a model of congenital central**
509 **hypoventilation syndrome.**

510 Congenital central congenital hypoventilation syndrome (CCHS) is a rare genetic disease is associated
511 with mutations of the PHOX2B gene and characterized by life-threatening breathing deficiencies
512 (Ceccherini, Kurek, & Weese-Mayer, 2022; Dubreuil et al., 2008). Phox2b is a transcription factor
513 required for the specification of the autonomous nervous system that contains respiratory control
514 centers. Because some of our preliminary observations strongly suggest a possible involvement of
515 microglia in the disease (unpublished data), we tested whether MorphoCellSorter highlighted
516 eventual morphological alterations of microglia in Phox2b mutants (CCHS embryos) compared to
517 wildtype embryos (WT), focusing on brainstem tissue that hosts respiratory networks involved in
518 breathing rhythmogenesis.

519 In this case using a threshold of 0.8, the PCA highlighted 12 parameters that were used to rank
520 microglia with Andrews plots: circularity, ramification index, perimeter area ratio, skeleton
521 processes ratio, fractal dimension, processes cell areas ratio, density, branching index, processes cell
522 areas ratio, convexity, lacunarity and solidity (Supp. Fig. 5A-C). These parameters were weighted to
523 generate the Andrews plots (Supp. Fig. 5D) used to rank the cells according to their morphology (Fig.
524 5B; complete ranking in Supp. Fig. 6).

525 Both populations displayed a large variability of morphologies from amoeboid to few ramified
526 processes and were well represented throughout the ranking (Fig. 5B). This is concordant with
527 previous studies on developing microglia: they can concomitantly be found in a large variety of
528 shapes and morphologies (Orłowski, Sołtys, & Janeczko, 2003). Indeed, the distributions of Andrews
529 scores showed no difference between WT and mutant mice. The overlap of distributions between
530 the populations found was 78.9% (Fig. 5C). Accordingly, when taking into consideration the various
531 morphological indices, there was no significant difference between WT and Phox2b mutant
532 microglial morphologies (Fig. 5D-W). Additional experiments are required to test whether this is
533 specific for embryonic stages and whether this is associated or not to different microglial functional
534 states.

535 **Discussion**

536 MorphoCellSorter enables the automated measurement of morphological descriptors, the
537 calculation of several non-dimensional indices, and a meaningful comparison of cell populations
538 based on their morphological characteristics. The method was initially applied to an ischemic stroke
539 model on confocal images with significant morphological changes. MorphoCellSorter was
540 subsequently tested on five different datasets with heterogeneous characteristics (various models,
541 age, sex, imaging technique and type of collected signal), showcasing its adaptability. We then
542 successfully used our approach to compare the cells' morphology in an Alzheimer's disease context,
543 and in embryonic microglia using a CCHS model. Our method can autonomously identify the most
544 effective parameters for discriminating the studied cell set, thereby providing valuable insights into
545 microglial morphology. Additionally, it offers a useful automated ordering of cells based on a
546 combination of selected parameters using Andrews plots. This feature allows for precise positioning
547 of cells along an axis, ranging from round cells to highly branched cells, facilitating the discrimination
548 of various cell populations based on their morphologies.

549 The use of the Andrews plots offers the possibility to combine all automatically selected most
550 discriminant parameters and to weight them according to their relevance, making the rankings more
551 accurate and less subjective than only sorting the cells based on one parameter. Even if we
552 recommend a threshold at 0.8 for the number of parameters selected, as it gave good rankings for all
553 datasets we tested, we included the possibility to change this threshold if the generated ranking is
554 not satisfying, knowing that all thresholds give accurate rankings when compared to expert rankings.

555 The automated parameter selection relies on principal component analysis, which is used to
556 determine the parameters that best disperse the data. In contrast, other approaches use PCA for
557 dimensionality reduction to create new morphological parameters that are difficult to apprehend as
558 they do not refer to any physical measure (Clarke et al., 2021; Heindl et al., 2018; Salamanca et al.,
559 2019). The strength of MorphoCellSorter lies in its personalized approach, with automated

560 parameter selection adapted to the dataset, making it easily applicable to segmented microglia in
561 diverse contexts, including those with distinct morphologies, such as microglia in culture or *in vivo*
562 acquisitions. It does not require program adaptation or the need to train a neural network for
563 deep/machine learning approaches. We observed that some selected parameters were consistent
564 between all the tested datasets (ramification index and perimeter area ratio for example), showing
565 their robustness to differentiate microglial cells with various morphologies. On the contrary, some
566 parameters were never selected (inertia and linearity for example). The information contained in
567 these parameters were not discriminant enough in the datasets we used in this present work, but we
568 can imagine that they would have been selected if we would have chosen a model in which microglial
569 growth towards a specific site is observed, such as focal laser injury (Davalos et al., 2005; Haynes et
570 al., 2006).

571 We also introduce a ranking tool to further enhance morphological analysis. In contrast to recent
572 studies, we opt for ordering cells rather than classifying them. Microglial morphologies can span a
573 continuum with no clear boundaries between morphotypes. Automated clustering methods such as
574 k-means (Young & Morrison, 2018) may be more suggestive, as they require an *a priori*
575 determination of the number of clusters. Hierarchical clustering (Clarke et al., 2021) can avoid this
576 requirement but may result in non-reproducible clusters, or clusters without biological meaning.
577 Attempts to identify distinct morphotypes, as previously done with artificial intelligence (Leyh et al.,
578 2021), are also questionable due to varying definitions of morphotypes between laboratories and a
579 lack of consideration for subtle morphological differences and intermediate forms. This problem is
580 overcome by the ranking approach, as it does not lock the cells in defined categories but rather
581 position the cells in relation to one another. However, the ability to compare the evolution of
582 clusters of microglial morphologies in different conditions remains valuable, especially when
583 morphologies are heterogeneous in the same population, such as in developmental microglia or
584 pathological contexts. Comparing medians or means of certain parameters may not reveal
585 differences due to high variability, whereas comparing the evolution of the proportions of specific

586 morphotypes may provide more informative insights. The Andrews plots used to generate a ranking
587 of the cells could also be used to generate clusters of the cells presenting morphological
588 resemblances, as similar cells display similar Andrews curves' trajectories.

589 We chose not to integrate a segmentation tool into our program, as the segmentation method
590 should be tailored to the specific imaging conditions, materials, and microscopes used. Diverse
591 segmentation methods are available in different software, with varying levels of automation and
592 manual input requirements. Although, automated thresholding would be ideal. In our case, image
593 acquisitions were not entirely uniform, even within the same sample. For instance, in ischemic brain
594 samples, lipofuscin from cell death introduces background noise that can artificially impact threshold
595 levels. This effect is observed even when comparing contralateral and ipsilateral sides of the same
596 brain. In our experience, manually adjusting the threshold provides a more accurate, reliable, and
597 comparable selection of cellular elements, even though it introduces some subjectivity. To ensure
598 consistency in segmentation, we recommend that the same person performs the analysis across all
599 conditions. In this work, we present methods using FIJI. It is important to note that achieving perfect
600 cell segmentation is not a prerequisite for using MorphoCellSorter since the tool does not aim to
601 provide highly precise measurements of microglial morphology. For instance, discontinuous
602 processes are not problematic. Consequently, it is possible to work with lower-resolution
603 microscopes, such as epifluorescence wide-field microscopes, although the segmentation process
604 may be more labor-intensive if the source images are of lower quality. Obviously, the results of the
605 ranking will be highly affected by the quality and the homogeneity of segmentation in a given data
606 set. However, we did not assess how much the resolution of the microscope used could affects the
607 quality of the ranking as low resolution and poor signal to noise ratio would mainly affect the
608 segmentation step which is not the purpose of this paper.

609 One potential limitation is that we decided to work with 2D Z-stack projections, as accurate 3D
610 reconstructions are time-consuming and require high-resolution acquisitions. Our goal was to

611 develop a fast and robust method that could be broadly applicable to most microscopes and imaging
612 scenarios. Therefore, our approach may not yield precise measurements of parameters such as the
613 exact number and length of processes or their hierarchy. However, other research groups have
614 successfully developed tools capable of providing these types of measurements, such as 3DMorph
615 (York, LeDue, Bernier, & MacVicar, 2018) and MorphOMICS via Imaris (Colombo et al., 2022), Mic-
616 Mac (Salamanca et al., 2019). Instead, MorphoCellsorter is a rapid way to determine if a treatment,
617 genotype or location of cells affects morphology without going through the laborious work of 3D
618 reconstruction. Our tool can thus be complementary to methods that provide those precise metrics.

619 In summary, MorphoCellSorter is an efficient and user-friendly tool for morphological analysis that
620 operates with minimal computation time. The code is open-source on GitHub, accessible by the
621 community (https://github.com/Pascuallab/MorphCellSorter) and improved according to the needs.
622 It can be complemented with additional measures, such as the expression of specific markers, to
623 investigate the relationship between morphology and gene expression. The emergence of spatial
624 transcriptomics is a promising avenue for furthering our understanding of the link between
625 morphology and phenotype in the microglia field in which MorphoCellSorter will be of great interest.

626 **Figure legends**

627 **Figure 1: k-means clustering identifies highly different populations contralaterally vs ipsilaterally in**
628 **an ischemic stroke model but offers a heterogeneous cluster composition.**

629 **A** T2-weighted MRI acquisition of the tMCAO rat brain 24 hours after reperfusion (top). Z maximum
630 projections of IBA1 staining of microglia on the ipsilateral side to the lesion (bottom left) and
631 contralateral side (bottom right). Scale bar: 20 µm. **B** Scatter plot with each dot representing one
632 microglia from the complete dataset (ipsilateral and contralateral), plotted in function of their PC1
633 against PC2 values from the PCA conducted on all 20 initial morphological parameters. The colors
634 represent the clusters identified by the k-means method, and the 'x' symbols are the centers of each

635 cluster. **C** Sample of microglial cells and their affiliated cluster **D** Pie chart illustrating the
636 proportion of each cluster constituting the contralateral and ipsilateral sides.

637 **Figure 2**: **MorphoCellSorter approach to generate a ranking of the cells based on their morphology**
638 **applied to the ischemic stroke model on fixed tissue.**

639 **A** Summary of the fully automated MorphoCellSorter approach: morphological indexes of the
640 individualized and binarized microglia are computed on a first script (MorphoCellMeter), and the
641 resulting data table is used as an entry for MorphoCellSorter to generate the ranking of the cells
642 based on their morphological characteristics. **B** Cascade of normalized eigenvalues. The blue bars
643 represent the eigenvalues for each principal component (PCs), and the red curve is the cumulative
644 sum of the values. The first two eigenvalues corresponding to the first two PCs that account for over
645 70% of the total sum. **C** Correlation circle in the PC1 and PC2 planes. **D** Parameters ranked according
646 to their projection on PC1. Values are normalized by the highest projection value. To determine the
647 number of morphological parameters selected, here we consider the median number of the
648 normalized cumulative projection (pink curve), leading to a threshold at 0.5 (red line), and thus 7
649 kept parameters in this case. **E** Andrews plots generated with the 7 parameters weighted according
650 to their contribution onto PC1. Each curve represents one microglia in the high-dimensional space of
651 the 7 strongest parameters' projections onto PC1. The maximum variance between curves is
652 obtained at 359°.

653 **Figure 3: MorphoCellSorter offers a reliable ranking of microglia in an ischemic stroke model based**
654 **on their morphologies.**

655 **A** Automatic ranking generated by MorphoCellSorter of the 347 microglia constituting the ischemic
656 stroke model dataset. **B** Distribution of the rank difference between expert 1 manual and
657 MorphoCellSorter rankings. **C** Distribution of the rank difference between expert 2 manual and
658 MorphoCellSorter rankings. **D** Distribution of the rank difference between expert 1 and expert 2
659 manual rankings. **E** Correlation between expert 1 and MorphoCellSorter rankings. Spearman's

660 correlation coefficient Rs = 95968, p<0.0001. **F** Correlation between expert 2 and MorphoCellSorter
661 rankings. Spearman's correlation coefficient Rs = 97188, p<0.0001. **G** Correlation between expert 1
662 and expert 2 rankings. Spearman's correlation coefficient Rs = 93498, p<0.0001.

663 **Table 1: Evaluation of MorphoCellSorter rankings on highly heterogeneous datasets of microglia.**

664 The evaluation of the rankings is conducted by comparing the Spearman's correlation coefficients. w:
665 weeks, m: months, E: embryonic day, P: postnatal day, DIV: day *in vitro*, Ex: expert.

666 **Figure 4: MorphoCellSorter identifies morphological alterations in the visual cortex of APPxPS1-KI**
667 **mice.**

668 **A** Z maximum projections of IBA1 (microglia) and 4G8 (Aβ plaques) stainings of control and APPxPS1-
669 KI mice in the visual cortex. The white arrowheads point at Aβ plaques positive for 4G8, green
670 arrowheads designate ramified microglia far from Aβ plaques and red arrowheads point to highly
671 morphologically altered microglia close to Aβ plaques. Scale bar: 20µm. **B** MorphoCellSorter
672 automated ranking. Control microglia are represented in green and APPxPS1-KI microglia in orange. **C**
673 Distribution of the Andrews values at the maximum variance (Andrews scores) for control and
674 APPxPS1-KI microglia. **D-W** Morphological indexes computed by MorphoCellSorter. The data shown
675 are the mean ± standard deviation (std). Linear mixed models were applied when the application
676 conditions were respected and Wilcoxon tests were performed otherwise (for the Span Ratio) (N=3
677 mice for each condition, $n_{APP\text{-}PS1xKI}$ and $n_{Control}$ = 180). *p<0.05; **p<0.01; ***p<0.001.

678 **Figure 5: Accurate sorting of embryonic microglia reveals no morphological difference between**
679 **CCHS and WT embryos' microglia.**

680 **A** IBA1 stainings in WT and CCHS embryos' brainstems. **B** MorphoCellSorter automated ranking. WT
681 microglia are displayed in light purple and mutated microglia are represented in pink. Only every 3
682 microglia composing the dataset are displayed for readability purposes. **C** Distribution of the
683 Andrews scores for CCHS and WT microglia. **D-W** Morphological indexes computed by

684 MorphoCellSorter. The data's distribution is represented as well as the mean ± std. Linear mixed
685 models were applied (N_{WT}=5, N_{mutant}=4; n_{WT}=498 and n_{mutant}=444).

686 **Supplementary information**

687 **Supplemental figure 1: Parameters ranked according to their normalized projection onto PC1 for**
688 **the 5 tested datasets.**

689 Parameters ranked according to their projection onto PC1 for the following datasets: temporary
690 mean cerebral artery occlusion (tMCAo) on fixed tissue (**A**), permanent mean cerebral artery
691 occlusion (pMCAo) on live tissue (**B**), Alzheimer's disease (AD) model (**C**), embryonic microglia (**D**) and
692 microglia in culture (**E**). Values are normalized by the highest projection value. The number of
693 morphological parameters selected is determined by the threshold corresponding value of the
694 normalized cumulative projection selected (pink curve).

695 **Supplemental table 1: Identification of the optimal threshold.**

696 EM: Embryonic microglia, MC: Microglia in culture.

697 **Supplemental figure 2: Andrews plots at a 0.8 threshold.**

698 Andrews plots for the following datasets: temporary mean cerebral artery occlusion (tMCAo) on fixed
699 tissue (**A**), permanent mean cerebral artery occlusion (pMCAo) on live tissue (**B**), Alzheimer's disease
700 (AD) model (**C**), embryonic microglia (**D**) and microglia in culture (**E**).

701 **Supplemental figure 3: MorphoCellSorter rankings generated for the 5 datasets at a 0.8 threshold.**

702 **A** Ranking for the tMCAo fixed tissue data set, n=347 cells**. B** Ranking for the pMCAo live tissue data
703 set, n= 168 cells**. C** Ranking for the AD model data set, n=180 cells. **D** Ranking for the embryonic data
704 set, n=407 cells. **E** Ranking for microglia in culture data set, n=96

705 **Supplemental figure 4: Elaboration of MorphoCellSorter ranking for the AD dataset.**

706 **A** Cascade of normalized eigenvalues. **B** Correlation circle in the PC1 and PC2 planes. **C** Parameters
707 ranked according to their projection on PC1. Values are normalized by the highest projection value.
708 To determine the number of morphological parameters selected, we selected a threshold of 0.8 (red
709 line), and thus 11 kept parameters. **D** Andrews plots generated with the 11 parameters weighted
710 according to their contribution onto PC1. Each curve represents one microglia in the high-
711 dimensional space of the selected parameters' projections onto PC1. The maximum variance
712 between curves is obtained at 1°.

713 **Supplemental figure 5: Elaboration of MorphoCellSorter ranking for the CCHS dataset.**

714 **A** Cascade of normalized eigenvalues. **B** Correlation circle in the PC1 and PC2 planes. **C** Parameters
715 ranked according to their projection on PC1. Values are normalized by the highest projection value.
716 To determine the number of morphological parameters selected, here we used a threshold of 0.8
717 (red line), and thus 12 kept parameters. **D** Andrews plots generated with the 12 parameters
718 weighted according to their contribution onto PC1. Each curve represents one microglia in the high-
719 dimensional space of the selected parameters. The maximum variance between curves is obtained at
720 359°.

721 **Supplemental figure 6: MorphoCellSorter automated ranking of the CCHS dataset.**

722 WT microglia are displayed in light purple and mutated microglia are represented in pink.

723 **Supplemental figure 7: Pre-processing and segmentation procedure for all used datasets.**

724 Steps in grey were performed on FIJI, blue on MATLAB, yellow on ZEISS ZEN and purple on Procreate.

725 **Supplemental figure 8: Illustration of the 20 morphological indexes automatically computed.**

726

727 **Ethics approval and consent to participate**

728 Not applicable.

Consent for publication

Not applicable.

Availability of data and materials

The original code of MorphoCellSorter is available on GitHub (https://github.com/PascualLab/MorphocellSorter).

The datasets used during the current study are available from the corresponding author on reasonable request.

Competing interests

The authors declare that they have no competing interests.

Funding

This study is supported by research grants from Fondation pour la recherche médicale (reference DQ20170336751) and has been developed within the BETPSY project, which is supported by a public grant overseen by the French national research agency (Agence nationale de la recherche, ANR), as part of the second "Investissements d´Avenir" program (reference ANR-18-RHUS-0012). This work was also supported by the French National Research Agency within the framework of the LABEX CORTEX ANR-11-LABX-0042.

Authors' contributions

SB, SMD, PM, JC and OP conceptualized and designed the study. JC and OP were in charge of overall direction. The experiments were conducted by SB, MTB, LC, BP, GP CL, IH, VH, MW and SM. JH and OP secured the fundings. Coding was executed by SB, SMD, PM and JC. SB, PDG and KC participated in the analysis. All authors provided critical feedback and helped shape the research, analysis and

manuscript. SB and OP drafted the manuscript, and all authors provided critical review, commentary or revision.

Acknowledgments

We acknowledge the contribution of SFR Santé Lyon-Est (UAR3453 CNRS, US7 Inserm, UCBL) facility: CIQLE (a LyMIC member), especially Bruno Chapuis and Denis Ressnikoff for their help.

References

A, C. (2023). Hausdorff (Box-Counting) Fractal Dimension.

Adaikkan, C., Middleton, S. J., Marco, A., Pao, P. C., Mathys, H., Kim, D. N., . . . Tsai, L. H. (2019). Gamma Entrainment Binds Higher-Order Brain Regions and Offers Neuroprotection. *Neuron, 102*(5), 929-943.e928. doi:10.1016/j.neuron.2019.04.011

Adeluyi, A., Guerin, L., Fisher, M. L., Galloway, A., Cole, R. D., Chan, S. S. L., . . . Turner, J. R. (2019). Microglia morphology and proinflammatory signaling in the nucleus accumbens during nicotine withdrawal. *Science Advances, 5*(10), eaax7031. doi:10.1126/sciadv.aax7031

Ali, S., Liu, X., Queen, N. J., Patel, R. S., Wilkins, R. K., Mo, X., & Cao, L. (2019). Long-term environmental enrichment affects microglial morphology in middle age mice. *Aging, 11*(8), 2388-2402. doi:10.18632/aging.101923

Amiel, J., Laudier, B., Attié-Bitach, T., Trang, H., de Pontual, L., Gener, B., . . . Lyonnet, S. (2003). Polyalanine expansion and frameshift mutations of the paired-like homeobox gene PHOX2B in congenital central hypoventilation syndrome. *Nature Genetics, 33*(4), 459-461. doi:10.1038/ng1130

Andrews, D. F. (1972). Plots of High-Dimensional Data. *Biometrics, 28*(1), 125-136. doi:10.2307/2528964

Anttila, J. E., Whitaker, K. W., Wires, E. S., Harvey, B. K., & Airavaara, M. (2017). Role of microglia in ischemic focal stroke and recovery: focus on Toll-like receptors. *Progress in neuro-psychopharmacology & biological psychiatry, 79*(Pt A), 3-14. doi:10.1016/j.pnpbp.2016.07.003

Arganda-Carreras, I., Kaynig, V., Rueden, C., Eliceiri, K. W., Schindelin, J., Cardona, A., & Sebastian Seung, H. (2017). Trainable Weka Segmentation: a machine learning tool for microscopy pixel classification. *Bioinformatics, 33*(15), 2424-2426. doi:10.1093/bioinformatics/btx180

Bohlen, C. J., Bennett, F. C., & Bennett, M. L. (2019). Isolation and culture of microglia. *Current protocols in immunology, 125*(1), e70. doi:10.1002/cpim.70

Casas, C., Sergeant, N., Itier, J.-M., Blanchard, V., Wirths, O., van der Kolk, N., . . . Pradier, L. (2004). Massive CA1/2 neuronal loss with intraneuronal and N-terminal truncated Abeta42 accumulation in a novel Alzheimer transgenic model. *The American Journal of Pathology, 165*(4), 1289-1300. doi:10.1016/s0002-9440(10)63388-3

Ceccherini, I., Kurek, K. C., & Weese-Mayer, D. E. (2022). Developmental disorders affecting the respiratory system: CCHS and ROHHAD. *Handb Clin Neurol, 189*, 53-91. doi:10.1016/B978-0-323-91532-8.00005-7

Choi, S., Hill, D., Guo, L., Nicholas, R., Papadopoulos, D., & Cordeiro, M. F. (2022). Automated characterisation of microglia in ageing mice using image processing and supervised machine learning algorithms. *Scientific Reports, 12*(1), 1806. doi:10.1038/s41598-022-05815-6

Clarke, D., Crombag, H. S., & Hall, C. N. (2021). An open-source pipeline for analysing changes in microglial morphology. *Open Biology, 11*(8), 210045. doi:10.1098/rsob.210045

Colombo, G., Cubero, R. J. A., Kanari, L., Venturino, A., Schulz, R., Scolamiero, M., . . . Siegert, S. (2022). A tool for mapping microglial morphology, morphOMICs, reveals brain-region and sex-dependent phenotypes. *Nature Neuroscience, 25*(10), 1379-1393. doi:10.1038/s41593-022-01167-6

804 Davalos, D., Grutzendler, J., Yang, G., Kim, J. V., Zuo, Y., Jung, S., . . . Gan, W.-B. (2005). ATP mediates
805 rapid microglial response to local brain injury in vivo. *Nature Neuroscience, 8*(6), 752-758.
806 doi:10.1038/nn1472
807 Dubreuil, V., Ramanantsoa, N., Trochet, D., Vaubourg, V., Amiel, J., Gallego, J., . . . Goridis, C. (2008).
808 A human mutation in Phox2b causes lack of CO2 chemosensitivity, fatal central apnea, and
809 specific loss of parafacial neurons. *Proc Natl Acad Sci U S A, 105*(3), 1067-1072.
810 doi:10.1073/pnas.0709115105
811 Fernández-Arjona, M. d. M., Grondona, J. M., Granados-Durán, P., Fernández-Llebrez, P., & López-
812 Ávalos, M. D. (2017). Microglia Morphological Categorization in a Rat Model of
813 Neuroinflammation by Hierarchical Cluster and Principal Components Analysis. *Front Cell*
814 *Neurosci, 11*, 235. doi:10.3389/fncel.2017.00235
815 Fumagalli, S., Perego, C., Ortolano, F., & De Simoni, M.-G. (2013). CX3CR1 deficiency induces an early
816 protective inflammatory environment in ischemic mice. *Glia, 61*(6), 827-842.
817 doi:10.1002/glia.22474
818 García-Osorio, C., & Fyfe, C. (2005). Visualization of High-dimensional Data via Orthogonal Curves.
819 *JUCS - Journal of Universal Computer Science, 11*((11)), 1806-1819. doi:10.3217/jucs-011-11-
820 1806
821 Hanisch, U.-K., & Kettenmann, H. (2007). Microglia: active sensor and versatile effector cells in the
822 normal and pathologic brain. *Nat Neurosci, 10*(11), 1387-1394.
823 Haynes, S. E., Hollopeter, G., Yang, G., Kurpius, D., Dailey, M. E., Gan, W. B., & Julius, D. (2006). The
824 P2Y12 receptor regulates microglial activation by extracellular nucleotides. *Nat Neurosci,*
825 *9*(12), 1512-1519.
826 Heindl, S., Gesierich, B., Benakis, C., Llovera, G., Duering, M., & Liesz, A. (2018). Automated
827 Morphological Analysis of Microglia After Stroke. *Front Cell Neurosci, 12*.
828 doi:10.3389/fncel.2018.00106

Hristovska, I., Robert, M., Combet, K., Honnorat, J., Comte, J. C., & Pascual, O. (2022). Sleep decreases neuronal activity control of microglial dynamics in mice. *Nat Commun, 13*(1), 6273. doi:10.1038/s41467-022-34035-9

Hubert, V., Hristovska, I., Karpati, S., Benkeder, S., Dey, A., Dumot, C., . . . Wiart, M. (2021). Multimodal Imaging with NanoGd Reveals Spatiotemporal Features of Neuroinflammation after Experimental Stroke. *Adv Sci (Weinh), 8*(17), e2101433. doi:10.1002/advs.202101433

Hubert, V., Hristovska, I., Karpati, S., Benkeder, S., Dey, A., Dumot, C., . . . Wiart, M. (2021). Multimodal Imaging with NanoGd Reveals Spatiotemporal Features of Neuroinflammation after Experimental Stroke. *Adv Sci (Weinh), 8*(17), e2101433. doi:10.1002/advs.202101433

Jolliffe, I. T., & Cadima, J. (2016). Principal component analysis: a review and recent developments. *Philosophical Transactions. Series A, Mathematical, Physical, and Engineering Sciences, 374*(2065), 20150202. doi:10.1098/rsta.2015.0202

Kettenmann, H., Hanisch, U.-K., Noda, M., & Verkhratsky, A. (2011). *Physiology of Microglia* (Vol. 91).

Kongsui, R., Beynon, S. B., Johnson, S. J., & Walker, F. R. (2014). Quantitative assessment of microglial morphology and density reveals remarkable consistency in the distribution and morphology of cells within the healthy prefrontal cortex of the rat. *J Neuroinflammation, 11*, 182. doi:10.1186/s12974-014-0182-7

Leyh, J., Paeschke, S., Mages, B., Michalski, D., Nowicki, M., Bechmann, I., & Winter, K. (2021). Classification of Microglial Morphological Phenotypes Using Machine Learning. *Front Cell Neurosci, 15*, 701673. doi:10.3389/fncel.2021.701673

Madry, C., Kyrargyri, V., Arancibia-Cárcamo, I. L., Jolivet, R., Kohsaka, S., Bryan, R. M., & Attwell, D. (2018). Microglial Ramification, Surveillance, and Interleukin-1β Release Are Regulated by the Two-Pore Domain K+ Channel THIK-1. *Neuron, 97*(2), 299-312.e296. doi:10.1016/j.neuron.2017.12.002

853 Morrison, H., Young, K., Qureshi, M., Rowe, R. K., & Lifshitz, J. (2017). Quantitative microglia analyses
854 reveal diverse morphologic responses in the rat cortex after diffuse brain injury. *Scientific*
855 *Reports, 7*(1), 13211. doi:10.1038/s41598-017-13581-z
856 Nimmerjahn, A., Kirchhoff, F., & Helmchen, F. (2005). Resting microglial cells are highly dynamic
857 surveillants of brain parenchyma in vivo. *Science, 308*(5726), 1314-1318.
858 Orłowski, D., Sołtys, Z., & Janeczko, K. (2003). Morphological development of microglia in the
859 postnatal rat brain. A quantitative study. *International Journal of Developmental*
860 *Neuroscience: The Official Journal of the International Society for Developmental*
861 *Neuroscience, 21*(8), 445-450. doi:10.1016/j.ijdevneu.2003.09.001
862 Paolicelli, R. C., Sierra, A., Stevens, B., Tremblay, M.-E., Aguzzi, A., Ajami, B., . . . Wyss-Coray, T.
863 (2022). Microglia states and nomenclature: A field at its crossroads. *Neuron, 110*(21), 3458-
864 3483. doi:10.1016/j.neuron.2022.10.020
865 Plescher, M., Seifert, G., Hansen, J. N., Bedner, P., Steinhäuser, C., & Halle, A. (2018). Plaque-
866 dependent morphological and electrophysiological heterogeneity of microglia in an
867 Alzheimer's disease mouse model. *Glia, 66*(7), 1464-1480. doi:10.1002/glia.23318
868 R, B. (2023). Thresholding Tool.
869 Salamanca, L., Mechawar, N., Murai, K. K., Balling, R., Bouvier, D. S., & Skupin, A. (2019). MIC-MAC:
870 An automated pipeline for high-throughput characterization and classification of three-
871 dimensional microglia morphologies in mouse and human postmortem brain samples. *Glia,*
872 *67*(8), 1496-1509. doi:10.1002/glia.23623
873 Sierra, A., Abiega, O., Shahraz, A., & Neumann, H. (2013). Janus-faced microglia: beneficial and
874 detrimental consequences of microglial phagocytosis. *Front Cell Neurosci, 7*, 6.
875 doi:10.3389/fncel.2013.00006
876 T, V. (2023). Lacunarity of a binary image.

Tolle, C. R., McJunkin, T. R., & Gorsich, D. J. (2008). An efficient implementation of the gliding box lacunarity algorithm. *Physica D: Nonlinear Phenomena, 237*(3), 306-315. doi:10.1016/j.physd.2007.09.017

Verdonk, F., Roux, P., Flamant, P., Fiette, L., Bozza, F. A., Simard, S., . . . Danckaert, A. (2016). Phenotypic clustering: a novel method for microglial morphology analysis. *J Neuroinflammation, 13*, 153. doi:10.1186/s12974-016-0614-7

Vidal-Itriago, A., Radford, R. A. W., Aramideh, J. A., Maurel, C., Scherer, N. M., Don, E. K., . . . Morsch, M. (2022). Microglia morphophysiological diversity and its implications for the CNS. *Frontiers in Immunology, 13*, 997786. doi:10.3389/fimmu.2022.997786

York, E. M., LeDue, J. M., Bernier, L.-P., & MacVicar, B. A. (2018). 3DMorph Automatic Analysis of Microglial Morphology in Three Dimensions from Ex Vivo and In Vivo Imaging. *eNeuro, 5*(6), ENEURO.0266-0218.2018. doi:10.1523/ENEURO.0266-18.2018

Young, K., & Morrison, H. (2018). Quantifying Microglia Morphology from Photomicrographs of Immunohistochemistry Prepared Tissue Using ImageJ. *Journal of Visualized Experiments: JoVE*(136), 57648. doi:10.3791/57648

Zhang, S. (2019). Microglial activation after ischaemic stroke. *Stroke and Vascular Neurology, 4*(2), 71-74. doi:10.1136/svn-2018-000196

Figure 1

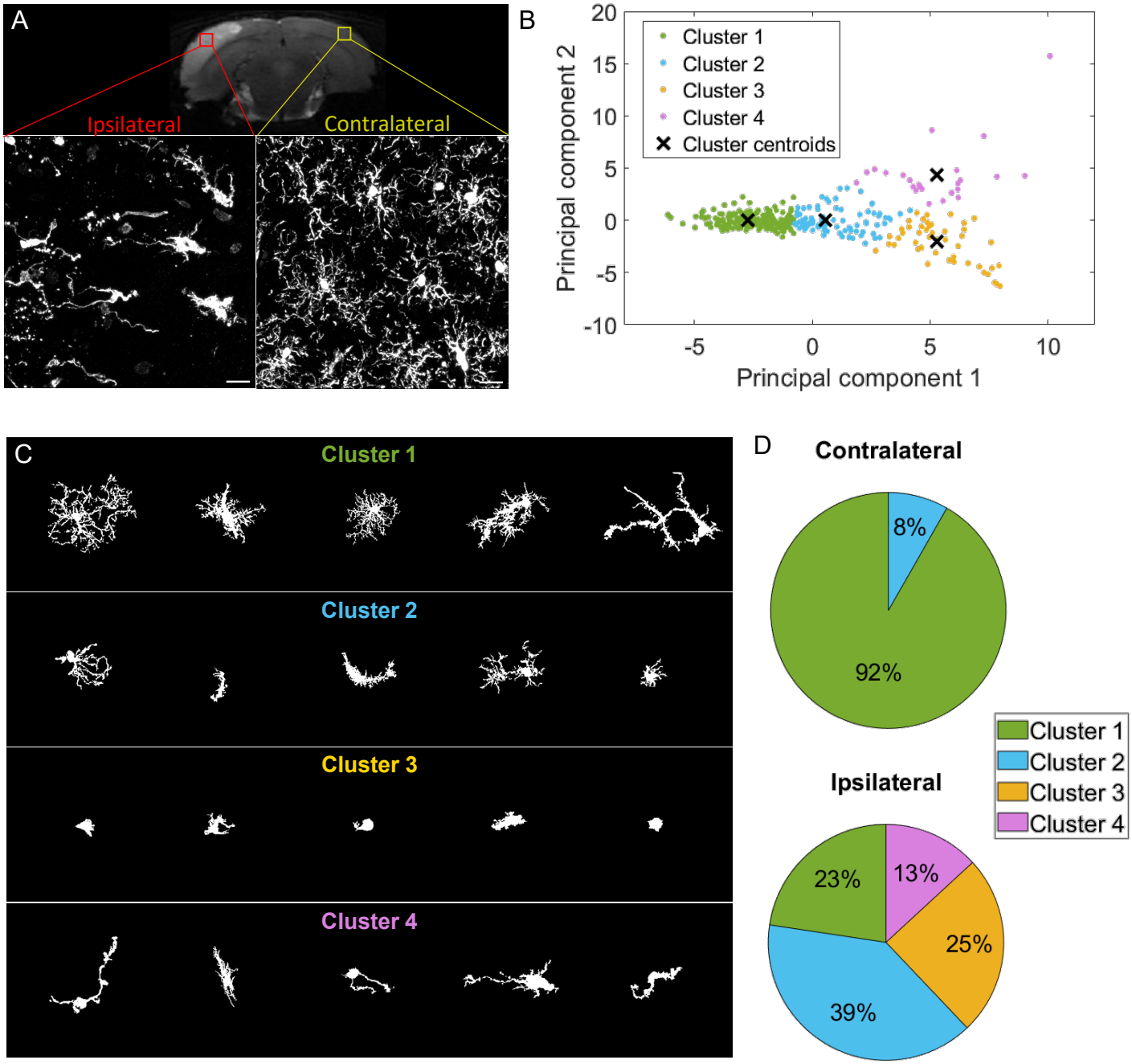
A
Ipsilateral
Contralateral
B
Cluster 1
Cluster 2
Cluster 3
Cluster 4
Cluster centroids
Principal component 2
Principal component 1
20
15
10
5
0
-5
-10
-5
0
5
10
C
Cluster 1
Cluster 2
Cluster 3
Cluster 4
D
Contralateral
8%
92%
Ipsilateral
23%
13%
25%
39%
Cluster 1
Cluster 2
Cluster 3
Cluster 4

Figure 2

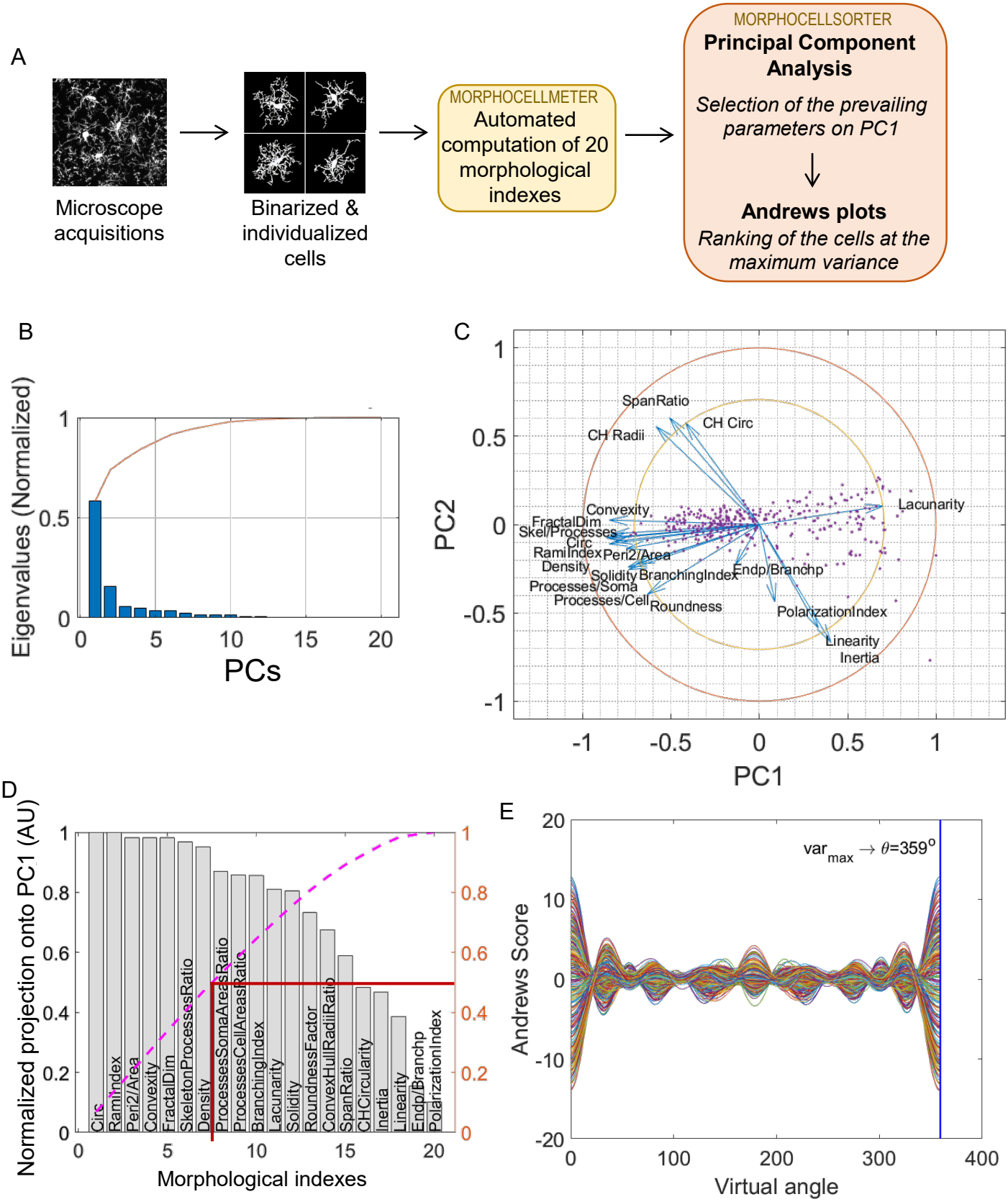
A
Microscope acquisitions
Binarized & individualized cells
MORPHOCELLMETER
Automated computation of 20 morphological indexes
MORPHOCELLSORTER
Principal Component Analysis
Selection of the prevailing parameters on PC1
Andrews plots
Ranking of the cells at the maximum variance
B
Eigenvalues (Normalized)
PCs
C
PC2
PC1
SpanRatio
CH Circ
CH Radii
Convexity
FractalDim
Skel/Processes
Circ
RamiIndex
Peri2/Area
Density
Solidity
BranchingIndex
Endp/Branchp
Processes/Soma
Processes/Cell
Roundness
PolarizationIndex
Lacunarity
Linearity
Inertia
D
Normalized projection onto PC1 (AU)
Morphological indexes
Circ
RamiIndex
Peri2/Area
Convexity
FractalDim
SkeletonProcessesRatio
Density
ProcessesSomaAreasRatio
ProcessesCellAreasRatio
BranchingIndex
Lacunarity
Solidity
RoundnessFactor
ConvexHullRadiiRatio
SpanRatio
CHCircularity
Inertia
Linearity
Endp/Branchp
PolarizationIndex
E
Andrews Score
Virtual angle
var max → θ=359°

Figure 3

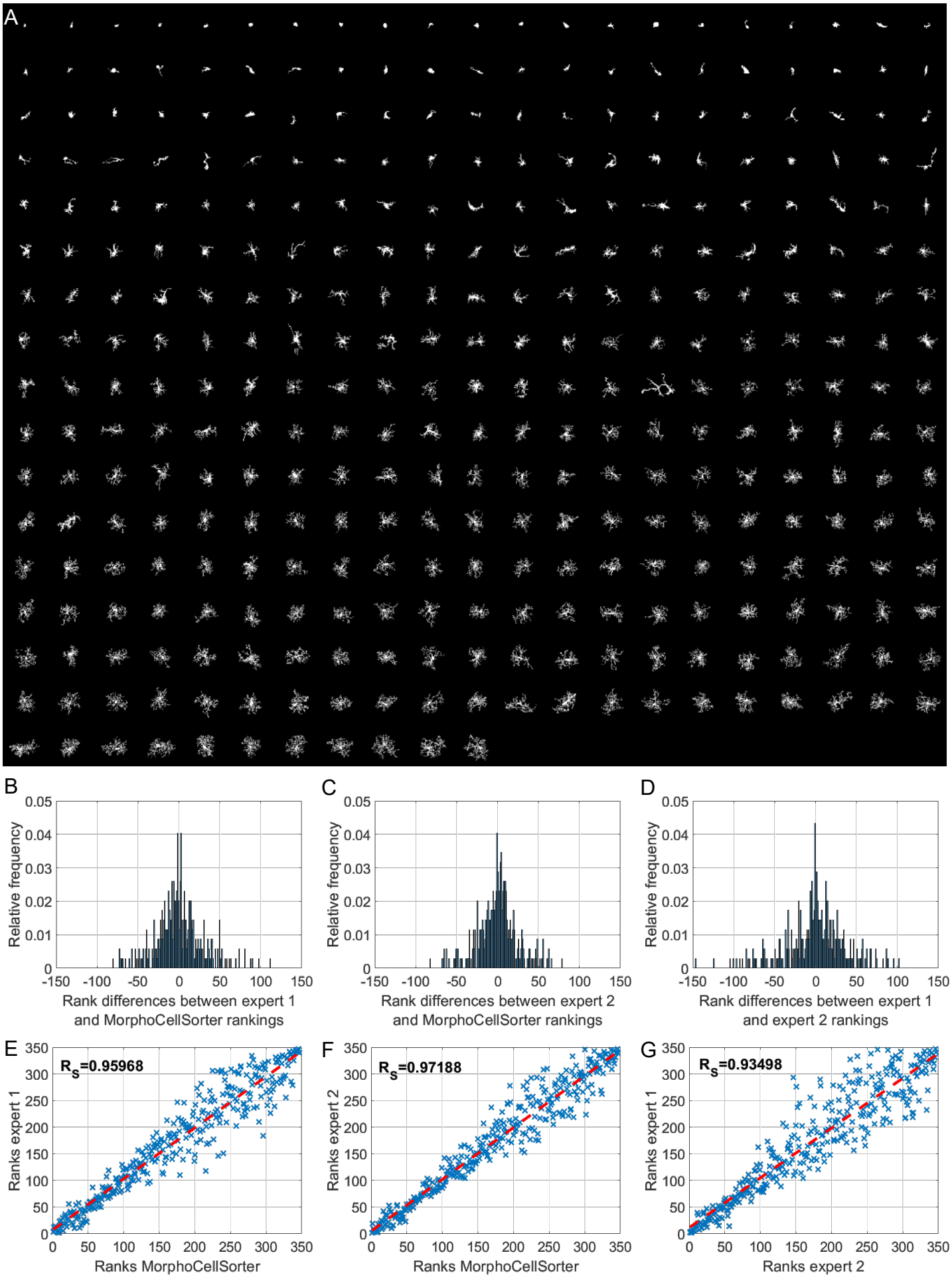
A
B
Relative frequency
Rank differences between expert 1 and MorphoCellSorter rankings
C
Relative frequency
Rank differences between expert 2 and MorphoCellSorter rankings
D
Relative frequency
Rank differences between expert 1 and expert 2 rankings
E
R_S=0.95968
Ranks expert 1
Ranks MorphoCellSorter
F
R_S=0.97188
Ranks expert 2
Ranks MorphoCellSorter
G
R_S=0.93498
Ranks expert 1
Ranks expert 2

Figure 4

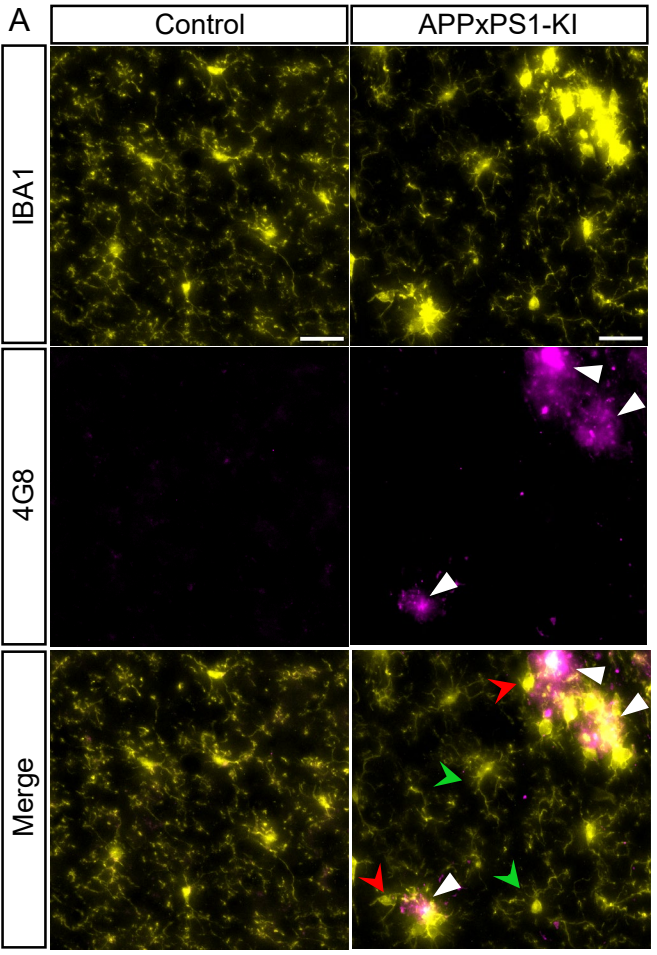
A
Control
APPxPS1-KI
IBA1
4G8
Merge

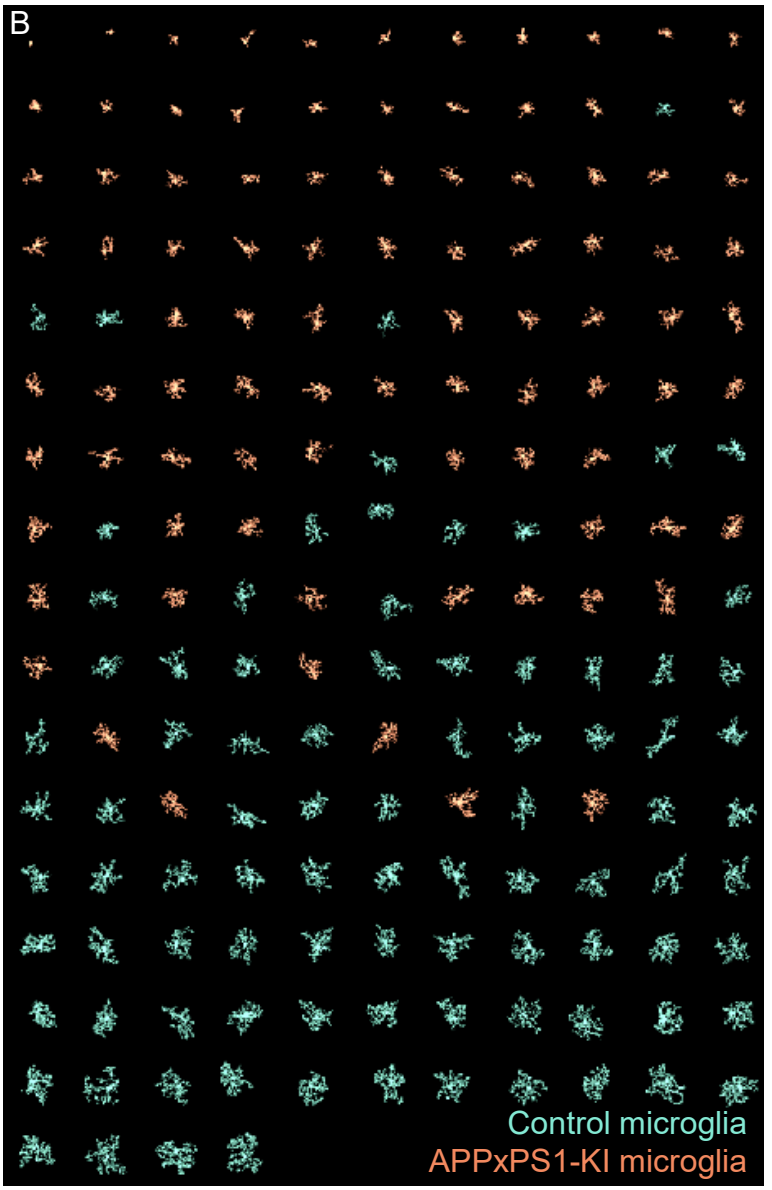
B
Control microglia
APPxPS1-KI microglia

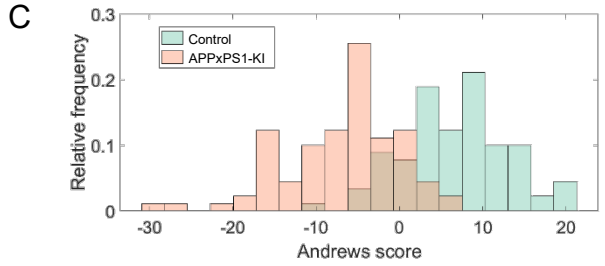
C
Control
APPxPS1-KI
Relative frequency
Andrews score

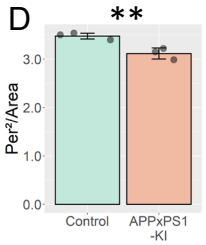
D
Per²/Area
Control
APPxPS1 -KI

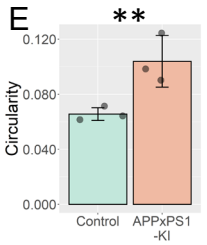
E
Circularity
Control
APPxPS1 -KI

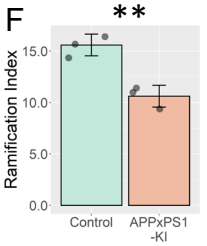
F
Ramification Index
Control
APPxPS1 -KI

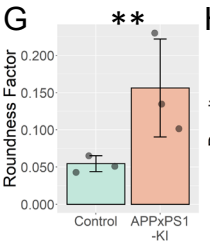
G
Roundness Factor
Control
APPxPS1 -KI

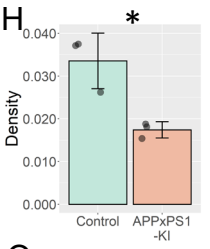
H
Density
Control
APPxPS1 -KI

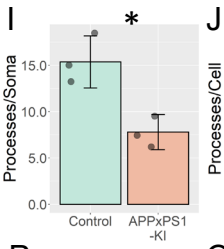
I
Processes/Soma
Control
APPxPS1 -KI

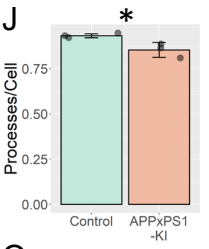
J
Processes/Cell
Control
APPxPS1 -KI

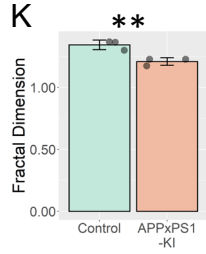
K
Fractal Dimension
Control
APPxPS1 -KI

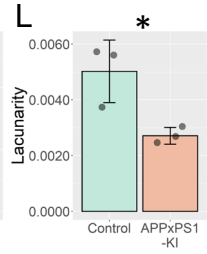
L
Lacunarity
Control
APPxPS1 -KI

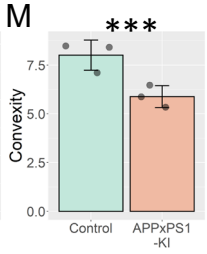
M
Convexity
Control
APPxPS1 -KI

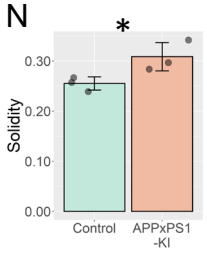
N
Solidity
Control
APPxPS1 -KI

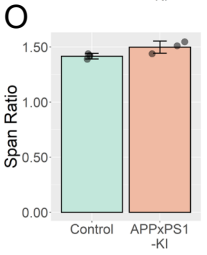
O
Span Ratio
Control
APPxPS1 -KI

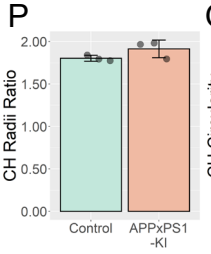
P
CH Radii Ratio
Control
APPxPS1 -KI

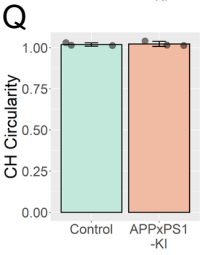
Q
CH Circularity
Control
APPxPS1 -KI

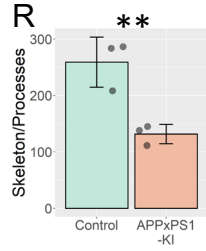
R
Skeleton/Processes
Control
APPxPS1 -KI

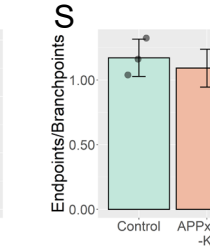
S
Endpoints/Branchpoints
Control
APPxPS1 -KI

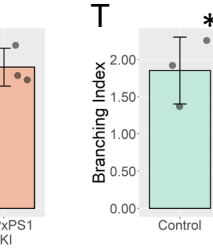
T
Branching Index
Control
APPxPS1 -KI

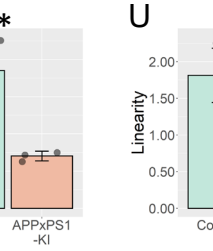
U
Linearity
Control
APPxPS1 -KI

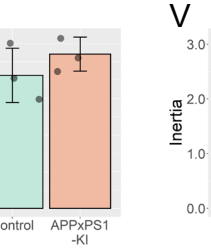
V
Inertia
Control
APPxPS1 -KI

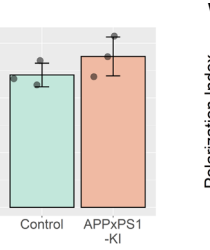
W
Polarization Index
Control
APPxPS1 -KI

Figure 5

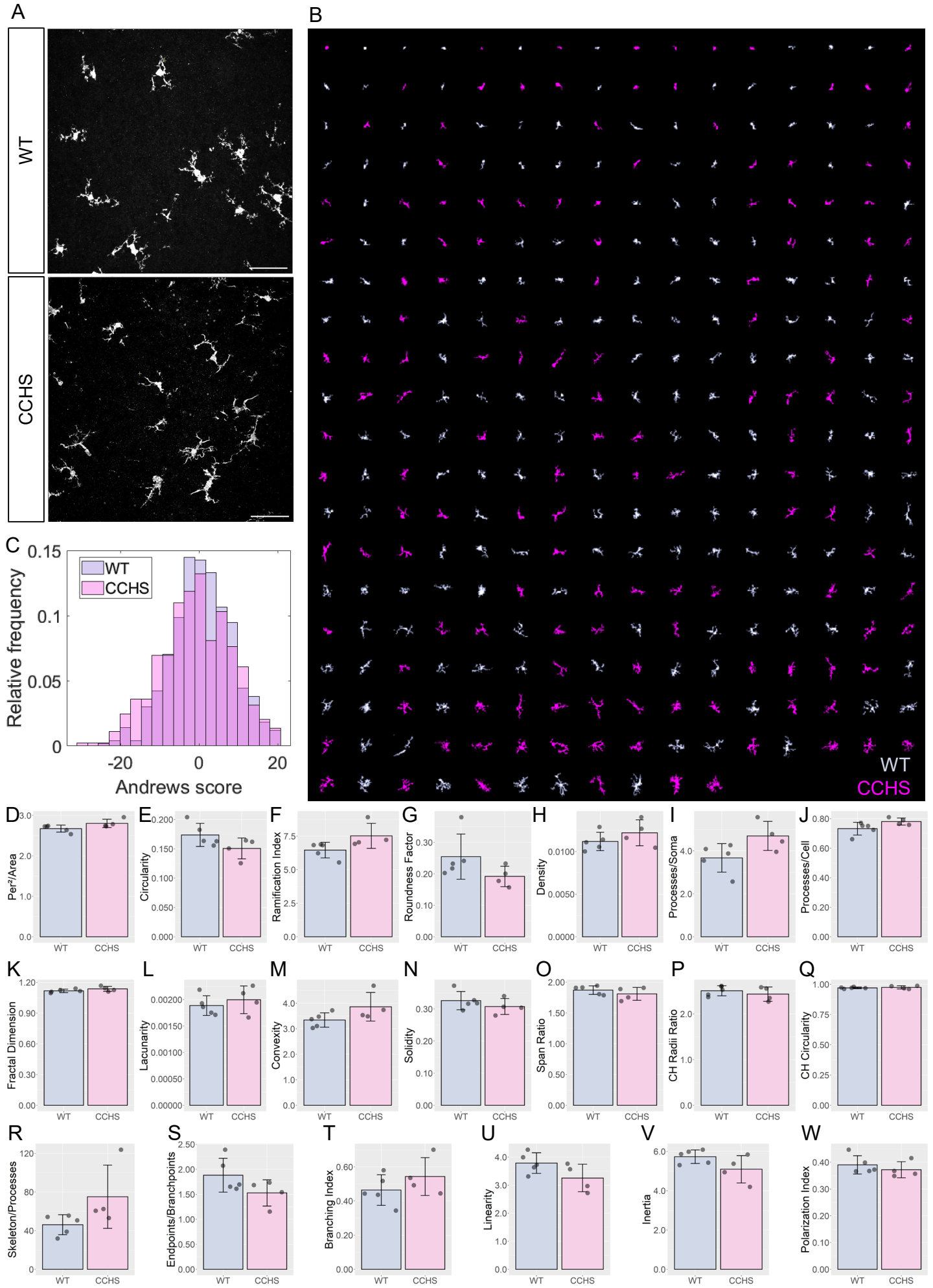
A
WT
CCHS
B
WT
CCHS
C
Relative frequency
Andrews score
WT
CCHS
D
Per²/Area
E
Circularity
F
Ramification Index
G
Roundness Factor
H
Density
I
Processes/Soma
J
Processes/Cell
K
Fractal Dimension
L
Lacunarity
M
Convexity
N
Solidity
O
Span Ratio
P
CH Radii Ratio
Q
CH Circularity
R
Skeleton/Processes
S
Endpoints/Branchpoints
T
Branching Index
U
Linearity
V
Inertia
W
Polarization Index